Statistical Study of SAR Transionospheric Autofocus Procedure

Patrick Haughey
Department of Mathematics
North Carolina State University
Raleigh, NC, United States
pmhaughe@ncsu.edu

Mikhail Gilman
Department of Mathematics
North Carolina State University
Raleigh, NC, United States
mgilman@ncsu.edu

Semyon Tsynkov
Department of Mathematics
North Carolina State University
Raleigh, NC, United States
stsynkov@ncsu.edu

2025 IEEE International Radar Conference (RADAR) | 979-8-3315-3956-6/25/$31.00 ©2025 IEEE | DOI: 10.1109/RADAR52380.2025.11031715

***Abstract*—Synthetic aperture radar (SAR) has been the imaging resource of choice for decades due to its all-weather capabilities and independence from external illumination. Orbital satellites that emit long-wavelength signals have the capacity to "see" through vegetation, snow, and ice. However, these systems are affected by the phase perturbations due to the ionospheric turbulence that phase shift the propagating radar signals, causing image distortions and blur.**

This study is a continuation of our previous work where we have developed an autofocus algorithm to improve the image quality deteriorated by the ionosphere. Here we conduct a statistical analysis of the efficiency of optimization-based SAR autofocus algorithm developed in our earlier publications. In particular, we test the limits and sensitivity of our autofocus algorithm that includes a gradient-based optimizer applied to a contrast-enhancing cost function. The role of perturbation factors, such as the intensity of the ionospheric turbulence, the average clutter reflectivity, and the average level of background noise, is investigated. Using the advantage of computer simulation, we are able to compare the initial corrupted image, as well as the autofocus outcomes, to the "true" image obtained with the perfect compensation of ionospheric distortions. The autofocus effectiveness is evaluated using three image quality metrics: normalized cross correlation (NCC), integrated side lobe ratio (ISLR), and the desynchronization of peak locations (PD). We find that our autofocus algorithm is capable of improving image quality and achieving a high level of similarity to the true image in most situations, with the high clutter level identified as the most challenging part of the setup.

***Index Terms*—Synthetic Aperture Radar (SAR), Autofocus, Ionosphere, Statistical Analysis, Normalized Cross Correlation**

I. Introduction

Synthetic aperture radar (SAR) is a powerful technology capable of providing imagery regardless of weather and time of the day. Low-frequency SAR systems have increased capacity for foliage, snow, and sand penetration. However, for orbital low-frequency SAR systems, the turbulence in the Earth's ionosphere causes random phase shifts that result in image distortions and blur. Besides that, SAR faces significant challenges, particularly from "clutter," or unwanted reflections, and noise from environmental and instrument sources, which can obscure target details. Autofocus techniques aim to correct the distortions and improve the image by estimating and mitigating phase errors caused by the environmental effects. Well-established autofocus methods, such as phase gradient autofocus (PGA) and map drift, are thoroughly described in the literature, see, e.g., [1]. Newer autofocus methods either enhance image sharpness or model sparse targets to approximate the corrupted signal [2]–[4]. Our approach combines these strategies by modeling the ionosphere as a thin phase screen and iteratively optimizing image sharpness, focusing on a few high-contrast point scatterers to improve computational efficiency.

Building on the previous work in [5], this study statistically evaluates our autofocus algorithm's robustness across varying environmental conditions. Using computer-generated data, we measure algorithmic success by comparing the autofocused image with the "true" image (i.e., the one where the phase perturbations due to the ionosphere have been perfectly compensated), assessing the similarity between the focused and true images, as well as peak sharpening and correction of peak locations.

In what follows, we present the mathematical foundation of SAR imaging and our ionospheric model and describe the experimental setup and data generation process. Next, we outline the optimization techniques used in our autofocus procedure, as well as the metrics that we employ to assess its effectiveness. Using these metrics, we analyze the factors contributing to the distortions. We conclude with insights on potential improvements to the autofocus algorithm.

II. Methodology

A. Governing Equations

Since the ionosphere affects the azimuthal resolution significantly more than the range resolution—by two orders of magnitude [6]—we use a simplified, range-compressed 1D SAR model that is formulated exclusively via the azimuthal coordinates. We nondimensionalize the azimuthal coordinates by the azimuthal resolution Δ_A:

$$\Delta_A = \frac{\pi R c}{\omega_0 L_{SA}},$$

This work is supported by the US Air Force Office of Scientific Research (AFOSR) under awards nos. FA9550-23-1-0101 and FA9550-24-1-0172. Additional support was provided by the NASA North Carolina Space Grant through the National Space Grant College and Fellowship Program Opportunities in NASA STEM (FY 2020–2024) under award no. 80NSSC20M0095 (CFDA: 43.008).

where R is the distance between the orbit and target, c is the speed of light, ω_0 is the (angular) carrier frequency, and L_{SA} is the synthetic aperture length.

For our SAR system, we transmit a linear chirp waveform where the retarded potential of the returned signal is as follows:

$$P\left(t - \frac{2|x-z|}{c}\right) \approx g(t)\exp\left(i\frac{\pi}{F}(x-z)^2\right). \quad (1)$$

Here $g(t) = \exp\left(-i\omega_0(t-2R/c) - \alpha(t-2R/c)^2\right)$, α is the chirp rate, x is the antenna track coordinate, z is the ground coordinate, and $F = L_{SA}/\Delta_A$ is the nondimensionalized length of the synthetic aperture. Given that our analysis is limited to the azimuthal dimension, we drop the factor $g(t)$ from the retarded potential (1) because it influences only the range resolution and is canceled out by matched filtering.

The received backscattered signal, $u(x)$, includes contributions from ground targets within the synthetic aperture. In the absence of noise, we express this signal as

$$u_{\text{clean}}(x) = \int_{\mathcal{Z}} \exp\left(i\frac{\pi}{F}(x-z)^2 - i\psi(x,z)\right)\nu(z)\,\mathrm{d}z, \quad (2)$$

where $\nu(z) = \nu_{\text{target}}(z) + \nu_{\text{clutter}}(z)$ is the ground scattering potential, $\psi(x,z)$ represents ionospheric phase shifts, and $\mathcal{Z} \coloneqq \{z : |z-x| \le F/2\}$.

To reconstruct the image, we apply a matched filter and introduce a phase correction term $\psi^{\text{rec}}(x,y)$ to mitigate ionospheric distortion, yielding:

$$\mathcal{I}^{\text{rec}}(y) = \int_{\mathcal{X}} \exp\left(-i\frac{\pi}{F}(x-y)^2 + i\psi^{\text{rec}}(x,y)\right) \cdot w(x,y)\,u(x)\,\mathrm{d}x, \quad (3)$$

where $w(x,y)$ is a parabolic window normalized by its mean (Welch window), and $\mathcal{X} \coloneqq \{x : |x-y| \le F/2\}$. The reconstructed image, $\mathcal{I}^{\text{rec}}(y)$, serves as an approximation for the true image $\mathcal{I}(y)$ which is itself an approximation of the ground reflectivity $\nu(z)$.

B. Ionospheric Phase Screen Model

The ionosphere is a turbulent region with variable number density of charged particles. It is quite common to model the ionosphere as an infinitely thin phase screen placed between the satellite's flight path and the ground [7]. This phase screen maps a pair of antenna and target coordinates (x,z) to the phase perturbation $\Psi(s)$ via $s \equiv s(x,z) = \xi x + (1-\xi)z$. The latter expression for $s(x,z)$ represents the intersection between a straight ray path connecting x and z with the phase screen plane located at the elevation ξ, $\xi \in [0,1]$, relative to the orbit altitude. Hence, the perturbation and correction phases in (2) and (3) are given by $\psi(x,z) = \Psi\big(s(x,z)\big)$ and $\psi^{\text{rec}}(x,y) = \Psi^{\text{rec}}\big(s(x,y)\big)$, respectively.

We represent the ionospheric turbulence using a spectral model for $\Psi(s)$ that reflects the dissipation of energy at higher spatial frequencies [8], [9]. This behavior is modeled by constructing the phase perturbation as a truncated Fourier series:

$$\begin{aligned}\Psi(s) &\coloneqq \Re\left(\sum_{n=1}^{N} a_n e^{i(k_n s+\varphi_n)}\right)\\ &= \sum_{n=1}^{N} p_n\cos(k_n s) + q_n\sin(k_n s),\end{aligned} \quad (4)$$

where $p_n = a_n\cos(\varphi_n)$, $q_n = -a_n\sin(\varphi_n)$, N is the number of harmonics, and k_n represents the wave number of the n-th harmonic. The fundamental frequency of the Fourier series is scaled to the nondimensionalized synthetic aperture length F, setting the longest wavelength to $l_{\max} = \rho F$ for some $\rho > 0$; note that this is a modeling choice rather than a strict physical requirement. The wavenumber spectrum is then defined as $k_n = 2\pi n/l_{\max}$. To create stochastic realizations, we build a random vector of phase shifts by sampling a uniform distribution: $\{\varphi_n\}_{n=1}^{N} \sim \mathcal{U}(-\pi,\pi)$, while the amplitudes a_n represent a power-law decay: $a_n \propto k_n^{-2}$.

C. Experimental Setup

In our study we adopt the baseline setup from [5]. For the latter, we used the grid size $\delta_x = 0.25$, synthetic aperture length $F = 100$, and phase screen height $\xi = 0.5$. Three point scatterers, each with a unit reflectivity, are positioned within a spatial domain of 0 to 360 at arbitrary locations 144, 186, and 216. To assess autofocus robustness, we conduct three bulk simulations, in which we vary the following key parameters across 1,000 realizations.

- *Phase Screen Magnitude $\|\Psi\|_2$ and Phase Shifts*: Using the set of amplitudes $\{a_n\}_{n=1}^{6}$ from a baseline Ψ model from [5], we scale the magnitude $\|\Psi\|_2$ over 10 equally spaced levels from $\pi/5$ to 2π. Simultaneously, we sample a random vector of six phase shifts uniformly, $\{\varphi_n\}_{n=1}^{6} \sim \mathcal{U}(-\pi,\pi)$. For each of the 10 levels of $\|\Psi\|_2$, we generate 100 realizations of $\{\varphi_n\}_{n=1}^{6}$. In order to study the effect of $\|\Psi\|_2$ on the autofocus effectiveness, we fix the baseline realizations of clutter and noise across all 1,000 scenarios to isolate the effects of $\|\Psi\|_2$ and phase shifts.
- *Average Level of Clutter Reflectivity (σ_C)*: We generate 1000 realizations of $\sigma_C \in \frac{\sqrt{\pi}}{2}[0.01, 0.2]$ via Latin hypercube sampling. We define $X, Y \sim \mathcal{N}(0, 2\sigma_C^2/\pi)$ as independent random vectors such that $\nu_{\text{clutter}} \coloneqq \sqrt{\delta_x}(X+iY)$. The variance $\sigma^2 = 2\sigma_C^2/\pi$ corresponds to the Rayleigh distribution where $\sigma_C = \mathbb{E}(|X+iY|)$ represents the average clutter reflectivity. In this study we fix the baseline Ψ and noise while isolating only the effects of the level of clutter.
- *Average Level of Noise (σ_N)*: Similarly to the case of clutter above, we generate 1000 realizations with $\sigma_N \in \frac{\sqrt{\pi}}{2}[0.01, 0.2]$ via Latin hypercube sampling. We define the noise contribution as

$$u_{\text{noise}}(x) \coloneqq |\max(u_{\text{clean}}(x))| \cdot (X+iY),$$

where $X, Y \sim \mathcal{N}(0, 2\sigma_N^2/\pi)$, so that $\sigma^2 = 2\sigma_N^2/\pi$ models the average noise level relative to the maximum

level of the clean signal. We fix the baseline Ψ and clutter while isolating only the effect of noise.

D. Optimizing the Autofocus Cost Function

Our autofocus algorithm minimizes a cost function by estimating the optimal Fourier amplitudes $\{(p_n^{\text{rec}}, q_n^{\text{rec}})\}$ that represent Ψ^{rec} similarly to Ψ in (4). The cost function

$$\begin{aligned}\text{Cost}(\mathbf{p}^{\text{rec}}, \mathbf{q}^{\text{rec}}) = &-\delta_x \sum_i \left|\mathcal{I}\left(y_i; \Psi^{\text{rec}}(\mathbf{p}^{\text{rec}}, \mathbf{q}^{\text{rec}})\right)\right|^4 \\ &+ \zeta \sum_{n=1}^{N} k_n^2 \left((p_n^{\text{rec}})^2 + (q_n^{\text{rec}})^2\right)\end{aligned} \tag{5}$$

has two parts. The first term, $\|\mathcal{I}(y; \Psi^{\text{rec}})\|_4^4$, is consistent with the results of [10]; it enhances peak sharpness and minimizes the effect of the clutter. The second term is a regularization component that encourages the optimized Fourier amplitudes $a_n^{\text{rec}} = \sqrt{(p_n^{\text{rec}})^2 + (q_n^{\text{rec}})^2}$ to decrease with an increase of k_n. The regularization term is weighted by a parameter ζ.

We use the Broyden-Fletcher-Goldfarb-Shanno (BFGS) quasi-Newton optimization method, which approximates the Hessian matrix to improve convergence while avoiding the high computational cost of direct Hessian calculation. The gradient of the cost function is computed explicitly, and BFGS updates the Hessian approximation iteratively. We initialize the optimization with the Fourier amplitudes set to zero: $\{(p_n, q_n)_{n=1}^6\} = \{(0,0)_{n=1}^6\}$. Based on visual inspection of image quality across the initial tests, we set the regularization weight as $\zeta = 0.6$ because this value balances the peak sharpness with appropriate amplitude decay.

E. Measurement of Autofocused Image Quality

We evaluate image quality using computer-generated data, where the target structure is known. By setting the reconstruction amplitudes Ψ^{rec} to match the original Ψ, we obtain the best possible compensation of phase distortions, allowing the resulting image $\mathcal{I}$, that we call the true image, to serve as a benchmark. Minimizing our cost function yields an autofocused image $\mathcal{I}^{\text{rec}}$, which we compare to $\mathcal{I}$ using several quality metrics.

Our primary metric, the *normalized cross-correlation coefficient* (NCC), quantifies the structural similarity between $\mathcal{I}^{\text{rec}}$ and $\mathcal{I}$, allowing an azimuthal shift of up to $\pm\mu$:

$$\text{NCC}(\mathcal{I}, \mathcal{I}^{\text{rec}}; \mu) = \max_{u \in [-\mu, \mu]} \frac{\sum_i \Delta\mathcal{I}_i \Delta\mathcal{I}_i^{\text{rec}}(u)}{\sqrt{\sum_j \Delta\mathcal{I}_j^2 \sum_k \Delta\mathcal{I}_k^{\text{rec}}(u)^2}}, \tag{6}$$

where $\Delta\mathcal{I}_i := |\mathcal{I}(y_i)| - \overline{|\mathcal{I}|}$, and $\Delta\mathcal{I}_i^{\text{rec}}(u) := |\mathcal{I}^{\text{rec}}(y_i - u)| - \overline{|\mathcal{I}^{\text{rec}}|}$. Here, $\overline{|\mathcal{I}|}$ and $\overline{|\mathcal{I}^{\text{rec}}|}$ represent the mean intensities of the true image $\mathcal{I}$ and the reconstructed image $\mathcal{I}^{\text{rec}}$, respectively.

To further assess image quality, we compute the *integrated sidelobe ratio* (ISLR) [11], measuring peak sharpness relative to sidelobes. Each realization of $\nu(z)$ in (2) has $N_{\text{peaks}} = 3$ well-defined peaks located at $\{z_p\}_{p=1}^3$, so we identify three highest peaks of $\mathcal{I}^{\text{rec}}$, denote their locations by $\{y_p^{\text{rec}}\}_{p=1}^3$, and calculate ISLR as follows:

$$\text{ISLR} = 10 \log_{10}\left(\frac{E_{\text{sidelobes}}}{E_{\text{peaks}}}\right), \quad \text{where}$$

$$E_{\text{peaks}} = \sum_{p=1}^{N_{\text{peaks}}} \int_{|y - y_p^{\text{rec}}| \le 1} |\mathcal{I}^{\text{rec}}(y)|^2 \, \mathrm{d}y,$$

$$E_{\text{sidelobes}} = \left(\sum_{p=1}^{N_{\text{peaks}}} \int_{|y - y_p^{\text{rec}}| \le 20} |\mathcal{I}^{\text{rec}}(y)|^2 \, \mathrm{d}y\right) - E_{\text{peaks}}.$$

If Ψ and Ψ^{rec} were linear functions, the corrupted image would experience an azimuthal shift proportional to the slope differences between Ψ and Ψ^{rec} [1], [12]. However, our Fourier model may lead to non-uniform shifts in peaks across $\mathcal{I}^{\text{rec}}$. To quantitatively assess this phenomenon, we introduce the concept of peak desynchronization (PD). PD measures the variation in peak shifts between $\mathcal{I}$ and $\mathcal{I}^{\text{rec}}$ and is quantified by the standard deviation of the differences between the ordered sets of peak locations between $\mathcal{I}$ and $\mathcal{I}^{\text{rec}}$:

$$\text{PD}(\mathcal{I}, \mathcal{I}^{\text{rec}}) = \sigma\left(\{y_p^{\text{rec}} - y_p \mid p = 1, \ldots, N_{\text{peaks}}\}\right),$$

where y_p and y_p^{rec} are the ordered peak locations in $\mathcal{I}$ and $\mathcal{I}^{\text{rec}}$, respectively. A homogeneous shift of the peaks corresponds to $\text{PD} = 0$, while $\text{PD} > 0$ amounts to a geometrical distortion of the image.

III. Results

NCC was used as the primary metric to assess the similarity between the autofocused and true images, while allowing a uniform shift of up to ± 10. However, due to peak desynchronization (PD), NCC reaches a practical limit as shifting one peak closer to its true location can displace others, capping the achievable NCC.

Figure 1 illustrates NCC results across ten equidistant magnitudes of $\|\Psi\|$ from $\pi/5$ to 2π. The autofocus algorithm demonstrated robustness, achieving a median NCC of 0.82 across all realizations. We can observe a non-monotonic behavior of the median NCC as the level of $\|\Psi\|_2$ increases; this is due to the choice of the regularization weight (ζ) in (5): for $\zeta < 0.5$, the optimization algorithms performs better for $\|\Psi\|_2 > \pi$, and for $\zeta > 1$ the optimization performs better for $\|\Psi\|_2 < \pi$. For $\zeta = 0.6$, we strike a balance across $\|\Psi\|_2$: for $\|\Psi\|_2 = 2\pi$, a majority of realizations, 53 out of 100 realizations, achieved an NCC ≥ 0.75, confirming the algorithm's resilience under varying levels of ionospheric perturbation. This trend suggests that as intensity of phase perturbation increases, achieving high NCC values becomes more challenging.

Figure 2 shows the dependence of NCC on clutter levels, with σ_C ranging from 0.009 to 0.177. As clutter level σ_C increases, we observe a clear decline in the average NCC. For $\sigma_C \le 0.1$, 68% of scenarios achieve NCC ≥ 0.8, but for $\sigma_C > 0.1$, only 13% of scenarios reach NCC ≥ 0.8. The median NCC across all realizations is 0.76, with a median of NCC = 0.85 for $\sigma_C < 0.1$ and NCC = 0.59 for $\sigma_C >$

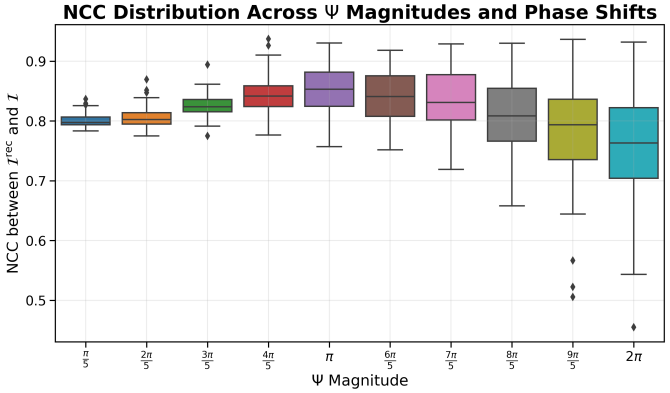

Fig. 1: Box plots of Normalized Cross-Correlation (NCC) for 100 realizations across 10 bins of $\|\Psi\|_2$, with an aggregate median NCC of 0.82 across all levels of ionospheric turbulence. The median NCC for $\|\Psi\|_2 \leq \pi$ is 0.82, and the median NCC for $\|\Psi\|_2 > \pi$ is 0.81, indicating robustness across ionospheric turbulence.

0.1. These findings highlight NCC's limitations in high clutter conditions, where clutter misalignment degrades image quality and underscores the importance of alternative metrics like PD to assess peak alignment.

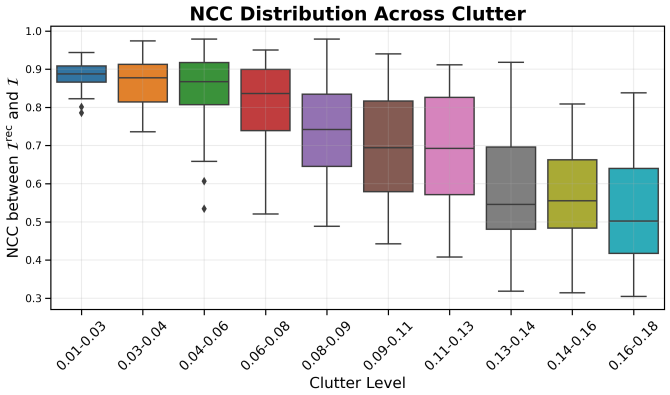

Fig. 2: Similar to Fig. 1, but for varying clutter level σ_C. For $\sigma_C \leq 0.1$, 68% of scenarios achieved NCC ≥ 0.8, while for $\sigma_C > 0.1$, only 13% reached NCC ≥ 0.8. The overall median NCC is 0.76, with medians of NCC = 0.85 for $\sigma_C < 0.1$ and 0.59 for $\sigma_C > 0.1$.

Conversely, noise has a minimal effect on image quality compared to clutter. For both realizations where $\sigma_N \leq 0.1$ and for $\sigma_N > 0.1$, the median NCC across these two ranges of noise remains 0.92. The middle 50% of NCC values (i.e., the interquartile range (IQR) of each box plot) across noise levels is also narrow, suggesting low variability in autofocusing outcomes due to noise. This stability indicates that the autofocus algorithm effectively averages out noise via matched filtering, making noise a negligible factor in limiting the quality of the reconstructed image.

The central hypothesis of this work is that minimizing the cost function improves image quality, yielding an autofocused image with sharper peaks that better resembles the true image. Using zero reconstruction Fourier amplitudes to build the initial corrupted image $\mathcal{I}^{\text{init}}$, we observed that reducing the cost function ultimately led to improvements of the resulting $\mathcal{I}^{\text{rec}}$ w.r.t. $\mathcal{I}^{\text{init}}$ in key metrics: Normalized Cross-Correlation (ΔNCC), Integrated Sidelobe Ratio (ΔISLR), and Peak Desynchronization (ΔPD).

Figure 3 illustrates that in most cases a decrease in the cost function correlates with enhanced image quality, with positive ΔNCC, negative ΔISLR, and negative ΔPD across a wide range of values of $\|\Psi\|_2$ and (σ_C). Notably, lower levels of the magnitude of phase perturbations are associated with minimal changes in the cost function, while higher magnitudes yield larger improvements in quality metrics.

For all levels of clutter, the autofocus algorithm seems well-suited to enhance the sharpness of the peaks; we observe 97%, 99.9% and 99% of ΔISLR < 0 for $\sigma_C = 0, 0.09$, and 0.177, respectively. While NCC improvement rates dropped from 98% at $\sigma_C = 0$ to 35% at $\sigma_C = 0.177$, ΔPD improvements also declined from 90% to 44%. This corroborates our earlier claim that high clutter levels limit the effectiveness of the autofocus algorithm. Overall, minimizing the cost function leads to enhanced image quality across various scenarios.

IV. Conclusions

This research shows that minimizing our cost function effectively enhances image quality by sharpening peaks and reducing geometrical distortions due to the ionospheric perturbations. While the autofocus process consistently improved the resulting images in the presence of ionospheric turbulence and noise, high clutter reflectivity (σ_C) remained a limiting factor, as shown by its relatively strong impact on peak desynchronization (PD).

Future enhancements of our methodology could involve clutter-mitigating terms in the cost function and dimensionality reduction strategies focused on key harmonics. These refinements would increase autofocusing robustness, potentially making SAR imaging more resilient to environmental disturbances.

References

[1] C. V. Jakowatz, D. E. Wahl, P. H. Eichel, D. C. Ghiglia, and P. A. Thompson, *Spotlight-Mode Synthetic Aperture Radar: A Signal Processing Approach*. Springer, 1996.

[2] T. Scarnati and A. Gelb, "Joint image formation and two-dimensional autofocusing for synthetic aperture radar data" *Journal of Computational Physic*, vol. 374, pp. 803–821, 2018.

[3] V. Churchill and A. Gelb, "Sampling-based spotlight SAR image reconstruction from phase history data for speckle reduction and uncertainty quantification" *SIAM/ASA Journal on Uncertainty Quantification*, vol. 10, no. 3, pp. 1225–1249, 2022.

[4] R. Morrison, M. Do, and D. Munson, "SAR image autofocus by sharpness optimization: A theoretical study," *IEEE Transactions on Image Processing*, vol. 16, pp. 2309–2321, 2007, doi: 10.1109/TIP.2007.903252.

[5] M. Gilman and S. V. Tsynkov, "Transionospheric autofocus for synthetic aperture radar," *SIAM Journal on Imaging Sciences*, vol. 16, no. 4, pp. 2144–2174, 2023.

[6] M. Gilman, E. Smith, and S. Tsynkov, *Transionospheric Synthetic Aperture Imaging*. Springer, 2017, ch. 4, sec. 4.3–4.4, pp. 183–193.

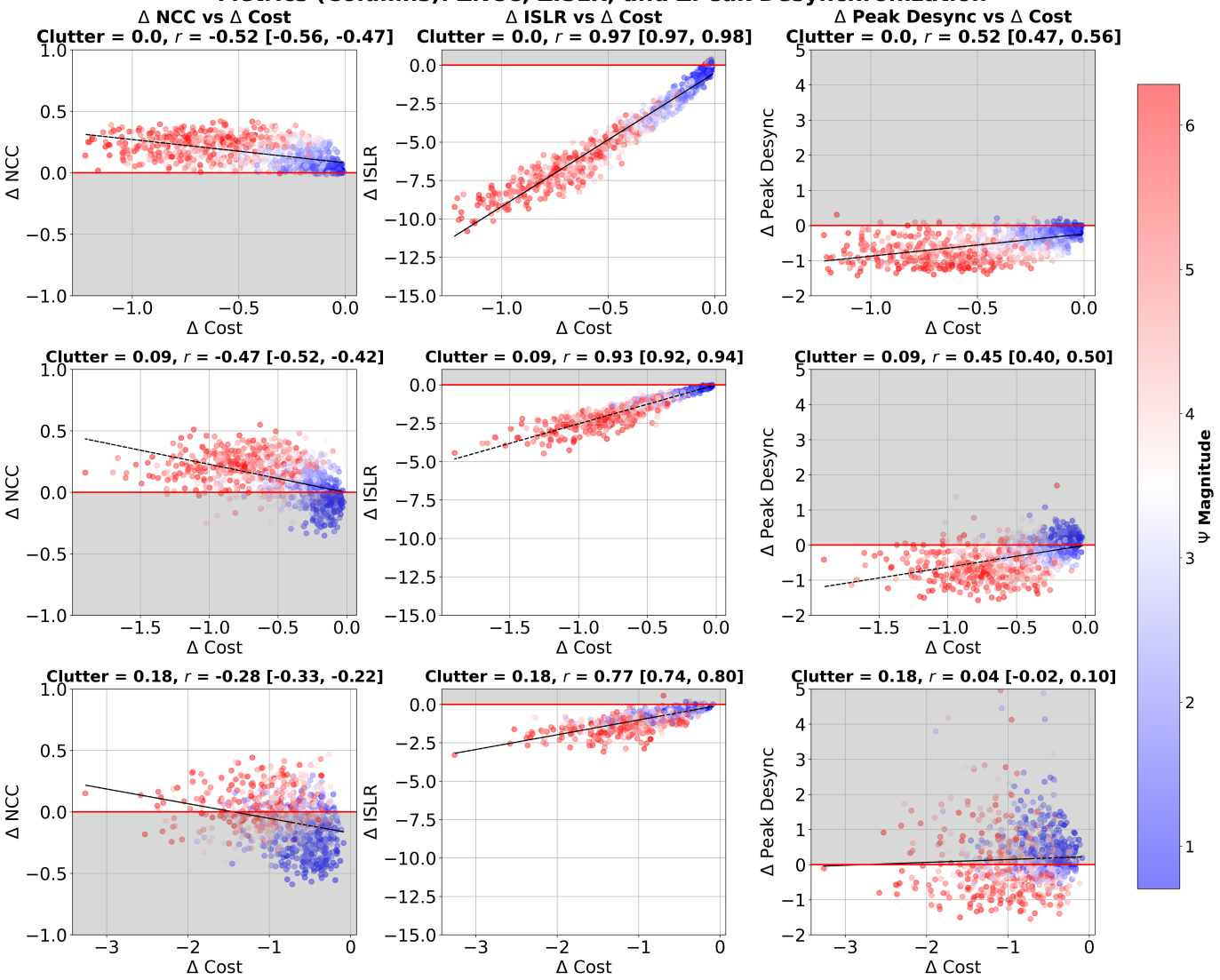

Fig. 3: Scatter plots of the changes of metric values resulting from cost minimization, with colors indicating increasing values of $\|\Psi\|_2$ from $\pi/5$ (blue) to 2π (red), for 1000 realizations per row. The points above the red line in the first column (ΔNCC) and below the red line in the second (ΔISLR) and third (ΔPD) columns indicate improvements. The improvement rate for NCC decreased from 98% to 35%, and that for PD, from 90% to 44% as σ_C increased from 0 to 0.177. The values and confidence intervals of the cross-correlation coefficient r between the changes of metrics and costs are shown in the subplot titles.

[7] M. Gilman and S. Tsynkov, "Modeling the Earth's ionosphere by a phase screen for the analysis of transionospheric SAR imaging," *IEEE Transactions on Geoscience and Remote Sensing*, vol. 62, pp. 1–16, 2023.

[8] G. Tagliaferro, A. Gatti, and E. Realini, "Sensing ionospheric turbulence using GNSS," in *EGU General Assembly 2020*, Online, May 4–8, 2020, EGU2020-8604. [Online]. Available: https://doi.org/10.5194/egusphere-egu2020-8604

[9] A. Glindemann, R. G. Lane, and J. C. Dainty, "Simulation of time-evolving speckle patterns using Kolmogorov statistics," *Journal of Modern Optics*, vol. 40, no. 12, pp. 2381–2388, 1993.

[10] J. Fienup and J. Miller, "Aberration correction by maximizing generalized sharpness metrics," *JOSA A*, vol. 20, pp. 609–620, 2003.

[11] I. G. Cumming and F. H. Wong, *Digital Processing of Synthetic Aperture Radar Data. Algorithms and Implementation*. Artech House, 2005.

[12] M. Gilman and S. Tsynkov, "Mathematical Analysis of SAR Imaging through a Turbulent Ionosphere" *Application of Mathematics in Technical and Natural Sciences: 9th International Conference for Promoting the Application of Mathematics in Technical and Natural Sciences — AMiTaNS'17*, vol. 1895, pp. 020003 (23pp), 2017.